

# CO, CO<sub>2</sub> and H<sub>2</sub> adsorption on ZnO, CeO<sub>2</sub>, and ZnO/CeO<sub>2</sub> surfaces: DFT simulations

Walter G. Reimers · Miguel A. Baltanás ·  
María M. Branda

Received: 30 December 2013 / Accepted: 23 April 2014  
© Springer-Verlag Berlin Heidelberg 2014

**Abstract** The adsorption of the molecules CO, CO<sub>2</sub>, and H<sub>2</sub> on several ceria and zinc oxide surfaces was studied by means of periodical DFT calculations and compared with infrared frequency data. The stable CeO<sub>2</sub>(111), CeO<sub>2</sub>(331), and ZnO(0001) perfect faces were the first substrates considered. Afterwards, the same surfaces with oxygen vacancies and a ZnO monolayer grown on Ceria(111) were also studied in order to compare the behaviors and reactivities of the molecules at those surfaces. The ceria surfaces were substantially more reactive than the ZnO surface towards the CO<sub>2</sub> molecule. The highest adsorption energy for this molecule was obtained on the CeO<sub>2</sub>(111) surface with oxygen vacancies. The molecules CO and H<sub>2</sub> both presented low or very low reactivities on all of the surfaces studied, although some reactivity was observed for the adsorption of CO onto the surfaces with oxygen vacancies, whereas H<sub>2</sub> exhibited reactivity towards the CeO<sub>2</sub>(111) surface with oxygen vacancies. This work was performed to provide a firm foundation for novel process development in methanol synthesis from carbon oxides, steam reforming of methanol for hydrogen production, and/or the water-gas shift reaction.

**Keywords** DFT · Zinc oxide · Ceria · Carbon monoxide · Carbon dioxide · Hydrogen · Adsorption

## Introduction

Recent UN Climate Change Conferences have predicted that fossil fuel usage will prevail throughout the present century, meaning that the accumulation of CO<sub>2</sub> and the resulting greenhouse effect require urgent attention. After signing up to the Kyoto treaty in 1997, several countries have decreased their net emissions of CO<sub>2</sub>. This has been possible because—at least, near point sources—CO<sub>2</sub> and CO can be recycled via chemical processes to produce liquid derivatives such as methanol and dimethyl ether, which are viable alternatives and intermediates to clean fuels [1–3]. Methanol, which is technologically and industrially relevant for the synthesis of several chemicals, is expected to play a key role in the next generation of renewable energy sources for use in fuel cells [4, 5], and also as a medium for H<sub>2</sub> storage and transportation.

Indeed, it is most probable that hydrogen will become the most efficient and clean fuel in the future [6], but this energy vector has serious disadvantages when utilized directly in automobiles due to transport and storage issues. An alternative solution to this problem is to use the catalytic synthesis of methanol as an intermediate, via steam reforming, to facilitate the production of H<sub>2</sub> in situ [7]. The water-gas shift (WGS) reaction CO<sub>2</sub> + H<sub>2</sub> ↔ CO + H<sub>2</sub>O is involved in both cases too.

Catalysts are used to increase the rate of a given chemical reaction. Despite the fact that the catalyst does not enter into the overall stoichiometric balance, its accelerating effect is generally due to the creation of a reaction pathway (usually multistep) that is characterized by a lower activation energy. Appropriate selection of the catalyst and reaction conditions makes it possible to lead the reaction along a preselected pathway to obtain the required product(s). The selectivity of a given catalyst fundamentally depends on the type of intermediates formed, and on their interactions with the surfaces present.

---

This paper belongs to Topical Collection QUITEL 2013

---

W. G. Reimers · M. M. Branda (✉)  
Instituto de Física del Sur, Departamento de Física (UNS/  
CONICET), Avda. Alem 1253, Bahía Blanca 8000, Argentina  
e-mail: cabranda@criba.edu.ar

M. A. Baltanás  
Instituto de Desarrollo Tecnológico para la Industria Química,  
INTEC (UNL/CONICET), Guemes 3450, Santa Fe S3000GLN,  
Argentina

When suitable supports are applied, palladium-based catalysts have been shown to excel in the hydrogenation of CO and CO<sub>2</sub> [8–12] to methanol. For the steam reforming of methanol in particular, systems based on Pd/ZnO show remarkable selectivity for CO<sub>2</sub>. Owing to their poor stability in fuel-cell applications, though, new supports have also been actively searched for [13]. In this regard, since the pioneering work of Iwasa et al. [14], it has been proven that the use of rare earth oxides increases both the thermal stability and long-term catalytic stability of Pd-ZnO under SRM conditions, even above 673 K [15]. A novel MSR catalyst consisting of palladium and zinc supported on promoted ceria was recently developed by the BASF Corporation, and exhibited remarkable catalytic performance in this process [16].

The importance of the processes that lead to the adsorption of the molecules CO, CO<sub>2</sub>, and H<sub>2</sub> onto ZnO and CeO<sub>2</sub> surfaces as well as onto other metallic oxides has been underlined by several works [2, 3]. Stampfl and coworkers studied the reactivities and reaction pathways of various intermediates during the synthesis of methanol on the polar ZnO (0001) surface by performing DFT calculations. They investigated the effect of surface coverage and found that a lower coverage is energetically more favorable [17]. The same surface, but with oxygen defects present, was also studied by Kiss et al. to characterize molecular adsorption during methanol synthesis. They found that O defects are active sites for CO and H<sub>2</sub> too. CO interacts strongly with oxygen vacancies on the ZnO (0001) surface, in particular at F<sup>2+</sup> sites [18]. When ZnO is used as the catalyst support, there are still some unanswered questions about the reaction mechanism that yields methanol. Under high-pressure conditions, methanol is formed from CO on Cu-free ZnO catalysts [19], but some experimental data indicate that CO<sub>2</sub> is the primary C source for generating the alcohol on Cu/ZnO/Al<sub>2</sub>O<sub>3</sub> [20].

Martins et al. [21, 22] studied the adsorption of CO and H<sub>2</sub> and also the dissociation of H<sub>2</sub> on ZnO using cluster models and Hartree–Fock calculations. They found that the CO molecule interacts with the surface of ZnO at sites representing the atoms with the lowest coordination number on the surface, and that the bond length changes slightly depending on the degree of charge transfer between the adsorbate and the superficial ZnO atoms.

Cerium oxides possess excellent properties for oxygen storage and release due to their ability to easily shift between the Ce<sup>3+</sup> and Ce<sup>4+</sup> oxidation states [23, 24]. Thus, CeO<sub>2</sub> is the most effective catalytic component for converting noxious exhaust gases from cars, and it is a key component in modern three-way catalysts (TWCs) [25].

In the last few years, there have been many studies of several aspects of bulk ceria and the reactivity of ceria surfaces from both theoretical and experimental perspectives [26–36]. Teschner et al. studied the adsorption of CO<sub>2</sub>, NH<sub>3</sub>, and CO on CeO<sub>2</sub> using infrared spectroscopy [37]. Even though these

authors used a hydrated ceria surface as substrate, they were able to detect the signal corresponding to CO physisorption, which is almost the same as the IR frequency of CO in the gas phase. Using DFT calculations, Chen et al. analyzed CO<sub>2</sub> adsorption on CeO<sub>2</sub>(110) [38]. They found that the most stable adsorption configuration involves the adsorption of the molecule parallel to the reduced CeO<sub>2</sub>(110) surface and near to an oxygen vacancy. They also found that the adsorbed molecule adopts an OCO angle of ~137° and shows C–O bond lengths of about ~1.2 and ~1.3 Å.

Fabris et al. studied the adsorption and oxidation of CO on CeO<sub>2</sub>(111) and (110) using DFT + U calculations. Their findings agreed with previous results in that they concluded that the CO molecule is physisorbed on the (111) face and chemisorbed on the more open (110) face of ceria [39]. They attributed this behavior to the surface formation of CO<sub>x</sub> complexes.

On this basis, in this paper we report a systematic analysis of the adsorption of CO<sub>x</sub> and H<sub>2</sub> on the surfaces of promising oxide co-catalysts, such as ZnO, CeO<sub>2</sub>, and ZnO, grown epitaxially onto ceria. We studied all of these adsorptions on the perfect surfaces and on the same surfaces but with oxygen defects. We believe that this kind of approach can substantially contribute to the construction of a comprehensive database to aid with novel process development in methanol synthesis from CO<sub>x</sub>, the steam reforming of methanol (SRM), and/or the WGS reaction.

## Computational details

We performed first-principles density functional calculations (DFT) for supercells representing different oxide surfaces. Periodic slab models and periodic plane-wave basis sets were used to study the adsorption of the CO, CO<sub>2</sub>, and H<sub>2</sub> molecules on the perfect surfaces of CeO<sub>2</sub>(111) and CeO<sub>2</sub>(331), CeO<sub>2</sub>(111) with oxygen vacancies, ZnO(0001) without or with oxygen vacancies, and ZnO/CeO<sub>2</sub>(111). The (111) and (331) faces were selected because they are the most stable surfaces of CeO<sub>2</sub> crystals [40] and, likewise, the polar ZnO(0001) surface was selected because of its relevance to both methanol synthesis and the water-gas shift reaction [17]. A monolayer of ZnO on CeO<sub>2</sub>(111) was also analyzed to compare its reactivity with those of the pure oxides. The ZnO monolayer was placed on an optimized slab representing the CeO<sub>2</sub>(111) surface. This monolayer was then geometrical-ly relaxed, together with the three nearest layers of CeO<sub>2</sub>.

The projector augmented wave (PAW) method [41] was used to represent the interaction between the valence electrons and the atomic cores. The one-electron state was expanded on a plane-wave basis set with a kinetic cutoff energy of 415 eV. A proper Monkhorst–Pack grid of special *k*-points was used for all calculations [42]. Considering the strong localization of the 4*f* electrons at the Ce<sup>+3</sup>, all calculations were performed

using the local density approximation (LDA +  $U$ ) and the generalized gradient approximation (GGA +  $U$ ), where  $U$  is the Hubbard parameter that penalizes double occupation of the  $4f$  orbital [43–47]. The optimal values of the Hubbard parameters selected by the LDA +  $U$  and GGA +  $U$  calculations were  $U = 5$  and  $U = 3$ , respectively, in agreement with previous DFT studies [32, 34, 48, 49]. The local density approximation (LDA +  $U$ ) was used to find the optimal geometry, and both the LDA +  $U$  and GGA +  $U$  approximations were used to calculate adsorption energies [50] and IR vibrational frequencies. Methfessel–Paxton smearing of width  $\sigma = 0.05$  eV was applied, and the reported total energies were then extrapolated to 0 eV [51]. The total energy threshold defining the self-consistency of the electron density was set to  $10^{-4}$  eV, and the convergence criterion for structural optimization was set to be such that the maximum force acting on each atom was less than 0.01 eV/Å. All calculations were carried out with the VASP code [52–56].

The size of the cell used to model the surface depended on the size and shape of the molecule to be adsorbed and the surface coverage to be studied. In this work, the perfect surface of CeO<sub>2</sub>(111) and the surface with oxygen vacancies were represented by 2×2 slabs with 9 atomic layers. The perfect surface of CeO<sub>2</sub>(331) was represented by a 2×1 slab with 18 atomic layers, and ZnO was represented by a 3×3 slab with 9 atomic layers. Finally, a slab with one layer of ZnO over the slab of CeO<sub>2</sub>(111) was built to represent ZnO grown epitaxially on CeO<sub>2</sub>(111). All the slab models were separated by >14 Å of vacuum.

Imposing periodic boundary conditions on the electrostatic potential of an asymmetric slab could give rise to an artificial electric field across the slab. Therefore, because the slabs analyzed in this work are not symmetric, we conducted single-point calculations using dipole correction to analyze possible changes in the adsorption energy [57, 58].

IR vibrational frequencies were calculated using a harmonic approach for the minimum of the potential energy. The corresponding Hessian dynamical matrix was calculated by a finite difference method where the atoms of the adsorbed molecules were independently displaced by  $\pm 0.015$  Å along each Cartesian coordinate direction. Afterwards, the harmonic molecular frequencies were obtained by diagonalizing the Hessian dynamical matrix.

## Results and discussion

This work is a follow-up to another study published by us at the beginning of this year, which mainly focused on the reactivity of the surfaces of pure oxides toward these

adsorbates as well as the charge distribution on the adsorbate(s) and surface(s) before and after adsorption [50]. The present work focuses instead on the infrared (IR) frequency data for all of the studied species and the relationships between these data, the geometries of the adsorbates, and their adsorption energies when adsorbed onto different ceria, ZnO, and ZnO/ceria surfaces. Therefore, although some of the adsorption energy ( $E_{\text{ads}}$ ) data we published previously are repeated in Table 1, it also shows new results on CeO<sub>2</sub>(111)vacO (“vacO” indicates that the surface contains oxygen vacancies) and on ZnO(0001)vacO. The optimized geometries of CO, CO<sub>2</sub>, and H<sub>2</sub> on all of the studied surfaces are displayed in Table 2. These molecules were initially placed at different surface sites; the reported geometries correspond to the most stable adsorption sites. Finally, the calculated IR vibrational frequencies are shown in Table 3. For comparison purposes, stretching frequency data for the free molecules are displayed in Table 4, which also includes values reported by Stamfl and coworkers (PBE calculations, [17]) and NIST (experimental IR data, [59]).

**Table 1** Adsorption energies (eV) of CO, CO<sub>2</sub>, and H<sub>2</sub>, as calculated using the LDA and GGA approaches for all of the surfaces investigated.  $E_{\text{ads}} = E(\text{molecule/surface}) - E(\text{free molecule}) - E(\text{surface})$

		$E_{\text{ads}}$ (LDA)	$E_{\text{ads}}$ (GGA)
CO	CeO <sub>2</sub> (111)	−0.21	+0.11
	CeO <sub>2</sub> (111)vacO <sup>c</sup>	−0.91	−0.27
	CeO <sub>2</sub> (111)vacO <sup>b</sup>	−0.23	+0.26
	CeO <sub>2</sub> (331)	−0.44	+0.34
	ZnO(0001)	−1.96	−1.28
	ZnO(0001)vacO <sup>a</sup>	−0.45	−0.01
	ZnO(0001)vacO <sup>b</sup>	−0.22	+0.38
	ZnO/CeO <sub>2</sub> (111)	−4.05	−5.51
CO <sub>2</sub>	CeO <sub>2</sub> (111)	−1.20	−0.37
	CeO <sub>2</sub> (111)vacO <sup>a</sup>	−1.85	−0.91
	CeO <sub>2</sub> (111)vacO <sup>b</sup>	−1.45	−0.75
	CeO <sub>2</sub> (331)	−1.18	−0.45
	ZnO(0001)	−0.09	+0.44
	ZnO(0001)vacO <sup>a</sup>	−0.12	+0.61
	ZnO(0001)vacO <sup>b</sup>	−0.60	+0.27
	ZnO/CeO <sub>2</sub> (111)	−0.65	+0.99
H <sub>2</sub>	CeO <sub>2</sub> (111)	−0.05	+0.01
	CeO <sub>2</sub> (111)vacO <sup>a</sup>	−0.31	−0.09
	CeO <sub>2</sub> (331)	−0.13	−0.07
	ZnO(0001)	−0.06	+0.06
	ZnO(0001)vacO <sup>b</sup>	−0.20	+0.11
	ZnO/CeO <sub>2</sub> (111)	−0.21	+0.26

<sup>a</sup> C is linked to a surface O near the vacancy

<sup>b</sup> O of the molecule occupies the hole generated by the oxygen vacancy

<sup>c</sup> C occupies the hole generated by the oxygen vacancy

**Table 2** Bond lengths and shortest distances from the adsorbed molecule to the surface, as calculated using the LDA approach

		Bond length in the adsorbate (Å)	Shortest distance from molecule to the surface (Å)	Geometrical characteristics
CO	CeO <sub>2</sub> (111)	1.14	C...O <sub>s</sub> = 2.91	C–O
	CeO <sub>2</sub> (111)vacO <sup>c</sup>	1.18	C...Ce = 2.64	C–O
	CeO <sub>2</sub> (111)vacO <sup>b</sup>	1.20	C <sub>e</sub> ...O = 2.63	C–O
	CeO <sub>2</sub> (331)	1.20	C...O <sub>s</sub> = 1.39	∠OCO = 121°
	ZnO(0001)	1.15	C...O <sub>s</sub> = 1.19	∠OCO = 180°
	ZnO(0001)vacO <sup>a</sup>	1.18	C...O <sub>s</sub> = 1.26	∠OCO = 141°
	ZnO(0001)vacO <sup>b</sup>	1.15	O...Zn = 2.57	C–O
	ZnO/CeO <sub>2</sub> (111)	1.15	C...O <sub>s</sub> = 1.18	∠OCO = 180°
	CeO <sub>2</sub> (111)	1.25–1.26	C...O <sub>s</sub> = 1.37	Planar CO <sub>3</sub> <sup>2-</sup>
	CeO <sub>2</sub> (111)vacO <sup>a</sup>	1.26–1.26	C...Ce = 2.61	∠OCO = 128°
	CeO <sub>2</sub> (111)vacO <sup>b</sup>	1.41–1.15	O...C <sub>e</sub> = 2.45	∠OCO = 121°
	CeO <sub>2</sub> (331)	1.21–1.30	C...O <sub>s</sub> = 1.39	Planar CO <sub>3</sub> <sup>2-</sup>
	ZnO(0001)	1.23–1.23	C...O <sub>s</sub> = 1.49	Planar CO <sub>3</sub> <sup>2-</sup>
	ZnO(0001)vacO <sup>a</sup>	1.17–1.20	C...O <sub>s</sub> = 2.08	∠OCO = 180°
	ZnO(0001)vacO <sup>b</sup>	1.15–1.19	O...Zn = 2.28	∠OCO = 180°
CO <sub>2</sub>	ZnO/CeO <sub>2</sub> (111)	1.25–1.25	C...O <sub>s</sub> = 1.31	Planar CO <sub>3</sub> <sup>2-</sup>
	CeO <sub>2</sub> (111)	0.77	H...O <sub>s</sub> = 2.25	H–H
	CeO <sub>2</sub> (111)vacO <sup>b</sup>	0.82	H...Ce = 2.56	H–H
	CeO <sub>2</sub> (331)	0.77	H...Ce = 2.87	H–H
	ZnO(0001)	0.78	H...O <sub>s</sub> = 2.17	H–H
	ZnO(0001)vacO <sup>a</sup>	0.77	H...O <sub>s</sub> = 2.03	H–H
	ZnO/CeO <sub>2</sub> (111)	0.78	H...O <sub>s</sub> = 1.92	H–H

<sup>a</sup> C is linked to a surface O near the vacancy

<sup>b</sup> O of the molecule occupies the hole generated by the oxygen vacancy

<sup>c</sup> C occupies the hole generated by the oxygen vacancy

**Table 3** Frequency values of the stretching modes of the adsorbed species, as calculated using the LDA approach

Adsorbed molecule	Substrate	Frequencies (cm <sup>-1</sup> ) <sup>d</sup>	Vibrational mode
CO	CeO <sub>2</sub> (111)	2155	$\nu_{C-O}$
	CeO <sub>2</sub> (111)vacO <sup>c</sup>	1804	
	CeO <sub>2</sub> (111)vacO <sup>b</sup>	1635	
	CeO <sub>2</sub> (331)	1733, 740	
	ZnO(0001)	2429, 1319	
	ZnO(0001)vacO <sup>a</sup>	2031, 103	
	ZnO(0001)vacO <sup>b</sup>	1954	
	ZnO/CeO <sub>2</sub> (111)	2207, 1413	
	CeO <sub>2</sub> (111)	1669, 1286	
	CeO <sub>2</sub> (111)vacO <sup>a</sup>	1610, 1251	
CO <sub>2</sub>	CeO <sub>2</sub> (111)vacO <sup>b</sup>	1785, 671	$\nu_{C-O}$
	CeO <sub>2</sub> (331)	1759, 1183	
	ZnO(0001)	1713, 1281	
	ZnO(0001)vacO <sup>a</sup>	2404, 1308	
	ZnO(0001)vacO <sup>b</sup>	2281, 1288	
	ZnO/CeO <sub>2</sub> (111)	1556, 1428	
	CeO <sub>2</sub> (111)	4070	
	CeO <sub>2</sub> (111)vacO <sup>a</sup>	3043	
	CeO <sub>2</sub> (331)	4080	
	ZnO(0001)	4041	
H <sub>2</sub>	ZnO(0001)vacO <sup>b</sup>	3996	$\nu_{H-H}$
	ZnO/CeO <sub>2</sub> (111)	4000	

<sup>a</sup> C is linked to a surface O near the vacancy

<sup>b</sup> O of the molecule occupies the hole generated by the oxygen vacancy

<sup>c</sup> C occupies the hole generated by the oxygen vacancy

<sup>d</sup> First value is for the symmetric stretching mode; second value is for the asymmetric stretching mode

**Table 4** Calculated and experimental stretching frequencies of the free molecules and ions

	Calculated frequency (cm <sup>-1</sup> )			Vibrational mode
	This work <sup>a</sup>	GGA-PBE [17]	Experimental [59]	
CO	2191	2146	2100	$\nu_{\text{C-O}}$
CO <sub>2</sub>	2424, 1354	2310, 1300	2350, 1350	$\nu_{\text{C-O}}$
CO <sub>3</sub> <sup>2-</sup>	1757, 1104	—	—	$\nu_{\text{C-O}}$
H <sub>2</sub>	4224	—	—	$\nu_{\text{H-H}}$
H <sub>2</sub> O	3835, 3718	3827, 3708	3650	$\nu_{\text{O-H}}$

<sup>a</sup> First value refers to the symmetric stretching mode; second value refers to the asymmetric stretching mode

## CO adsorption

The adsorption of CO is rather weak on the perfect surfaces of ceria, and the adsorbate only shows some reactivity when the carbon atom of CO is located on the oxygen vacancy in CeO<sub>2</sub>(111)vacO (see Fig. 1), with  $E_{\text{ads}}$  values of approximately -0.9 eV and -0.3 eV obtained using the LDA and GGA approaches, respectively. Nevertheless, considering that the calculated bond length in free C-O was 1.14 Å, it is clear from Table 2 that there is a significant decrease in C-O bond strength upon the adsorption of the molecule at both sites on CeO<sub>2</sub>(111) with O vacancies and on the stepped surface, CeO<sub>2</sub>(331), given that the impact of the adsorbate-surface interaction can be assessed by noting the lengthening of the C-O bond caused by the adsorption process. Such a change is typical of a significant charge-transfer interaction from the substrate to the antibonding  $\sigma^*(\text{C-O})$  orbital [60].

As the C-O bond length does not change on the perfect CeO<sub>2</sub>(111) surface but the adsorbate molecule does stretch at the two sites analyzed on CeO<sub>2</sub>(111)vacO (see Table 2), these stretches (i.e., C-O bond weakening) are correlated with decreases in  $\nu_{\text{C-O}}$ , with (down)shifts of ~400 and ~550 cm<sup>-1</sup> with respect to the free CO observed (see Tables 3 and 4).

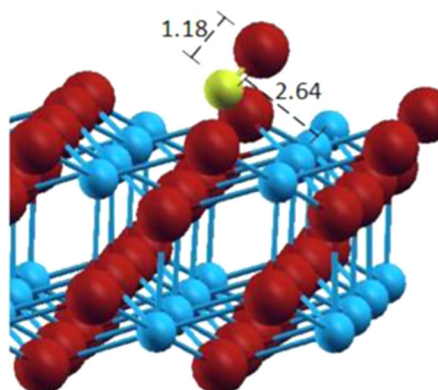


**Fig. 1** Adsorption of CO onto the CeO<sub>2</sub>(111)vacO surface. Blue spheres Ce atoms, red spheres O atoms, yellow spheres C atoms. Interatomic distances are in Å

In addition, the CO molecule binds to the stepped surface of ceria, CeO<sub>2</sub>(331), to generate CO<sub>2</sub>, but this species is deformed (its  $\angle\text{OCO}$  angle is 121° with respect to that of the linear free molecule; see Fig. 2). In this case, the  $\nu_{\text{C-O}}$  values are very similar to those calculated for the CO<sub>3</sub><sup>2-</sup> ion (Table 4).

On the other hand, CO binds to the surface oxygen atom to form linear CO<sub>2</sub> on almost all of the ZnO surfaces (see Table 2), and the  $\nu_{\text{C-O}}$  calculations yielded values that agree well with that of free CO<sub>2</sub> (see Tables 3 and 4). The only exception to this behavior occurs on ZnO(0001)vacO when the O of the molecule occupies the oxygen vacancy (see Fig. 3). Here, the value found for  $\nu_{\text{C-O}}$  is similar to but slightly smaller than the stretching frequency mode of the free CO molecule.

The CO molecule is strongly adsorbed onto the ZnO(0001) surface, and adsorbed very strongly indeed when ZnO is deposited epitaxially onto ceria, as seen in the ZnO/CeO<sub>2</sub>(111) entry in Table 1 (and Fig. 4). The substantial difference in the atomic structures of the Ce and Zn cations can explain this discrepancy, as electron retrodonation to the

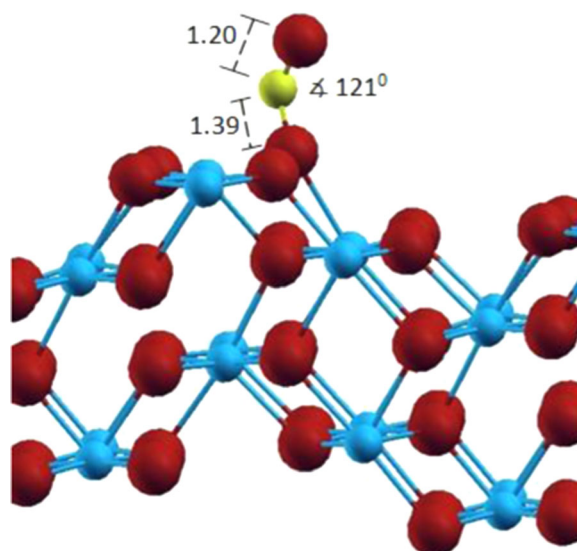


**Fig. 2** Adsorption of CO onto the CeO<sub>2</sub>(331) surface. Blue spheres Ce atoms, red spheres O atoms, yellow spheres C atoms. Interatomic distances are in Å



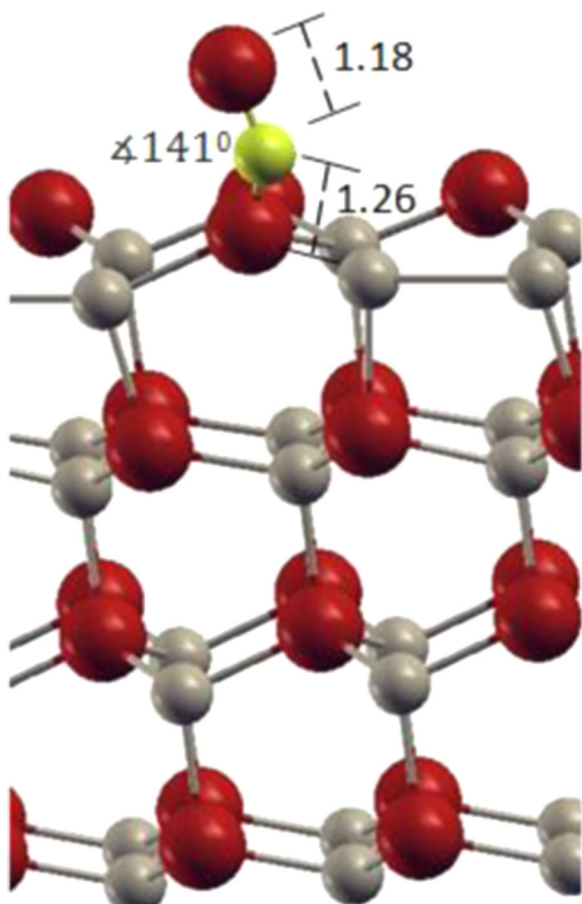


**Fig. 3** Adsorption of CO onto the ZnO(0001)vacO surface. Gray spheres Zn atoms, red spheres O atoms, yellow spheres C atoms. Interatomic distances are in Å

antibonding  $\sigma^*(\text{C}-\text{O})$  orbital is not expected from the latter. We must underline here that even though these LDA results

might overestimate  $E_{\text{ads}}$ , they are nevertheless a fairly good indicator of the relative adsorption tendencies of adsorbates, thus making them useful for comparing data among the different substrates (surfaces).

#### CO<sub>2</sub> adsorption

The ceria surfaces are much more reactive towards the CO<sub>2</sub> molecule than the ZnO surfaces are, with  $E_{\text{ads}}$  values of between  $-1.20$  and  $-1.85$  eV obtained using the LDA approach and values of between  $-0.37$  and  $-0.91$  eV obtained with the GGA approach (see Table 1). Planar CO<sub>3</sub><sup>2-</sup> species are obtained on all the perfect surfaces: CeO<sub>2</sub>(111), CeO<sub>2</sub>(331), and ZnO(0001), as well as on ZnO that is grown epitaxially onto ceria, ZnO/CeO<sub>2</sub>(111) (see Table 2 and Figs. 5 and 6). The values of the stretching frequency,  $\nu_{\text{C}-\text{O}}$ , are similar in all of these cases to that of the free CO<sub>3</sub><sup>2-</sup> ion, as observed from a comparison of Tables 3 and 4.

It is worth noting that the energetic stabilities of the adsorbate on the surfaces agree fairly well with the geometrical stability of the CO<sub>3</sub><sup>2-</sup> species: the geometries of CO<sub>3</sub><sup>2-</sup> on CeO<sub>2</sub>(111) and (331) and on ZnO/CeO<sub>2</sub>(111), for which we found C–O bond distances of between 1.31 and 1.39 Å, are very similar to that of the free species, whereas the chemisorbed species on ZnO(0001) has a distorted geometry with a C–O bond distance of 1.49 Å.

Nonetheless, the highest adsorption energies are found for both adsorption modes of CO<sub>2</sub> on CeO<sub>2</sub>(111)vacO (see Fig. 7), i.e., with either the carbon or the oxygen atom of the CO<sub>2</sub> molecule occupying the hole generated by the oxygen vacancy. In both cases, the adsorbed carbon dioxide accepts the electron pair from the hole and adopts the geometry of the

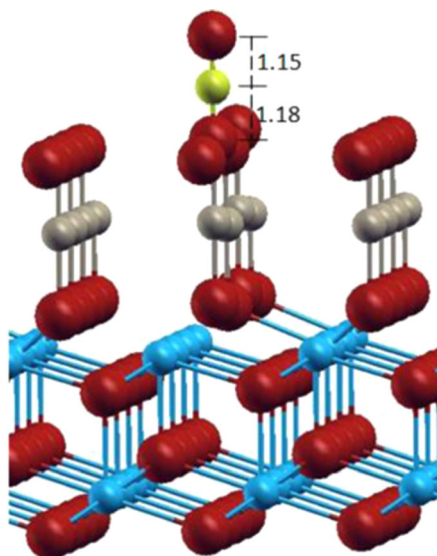


**Fig. 4** Adsorption of CO onto the ZnO/CeO<sub>2</sub>(111) surface. Gray spheres Zn atoms, blue spheres Ce atoms, red spheres O atoms. Interatomic distances are in Å

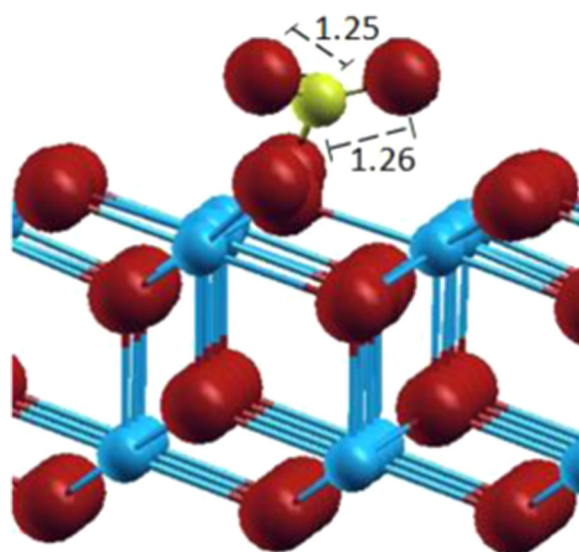


**Fig. 5** Adsorption of CO<sub>2</sub> onto the perfect CeO<sub>2</sub>(111) surface. Blue spheres Ce atoms, red spheres O atoms, yellow spheres C atoms. Interatomic distances are in Å

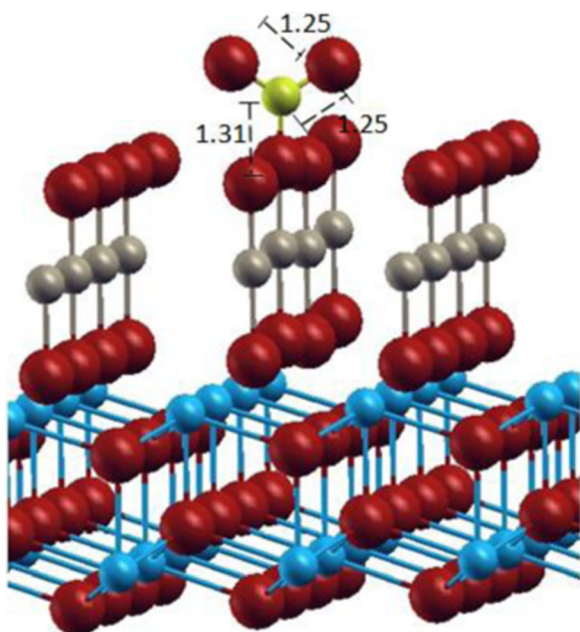


**Fig. 6** Adsorption of  $\text{CO}_2$  onto the  $\text{ZnO/CeO}_2(111)$  surface. Gray spheres Zn atoms, blue spheres Ce atoms, red spheres O atoms. Interatomic distances are in Å

$\text{CO}_3^{2-}$  ion, with an angle of  $\sim 120\text{--}128^\circ$  between the oxygen atoms (see Table 2 and Fig. 7). The calculated  $\nu_{\text{C-O}}$  values for  $\text{CeO}_2(111)\text{vacO}$  with the carbon of the  $\text{CO}_2$  molecule occupying the hole generated by the oxygen vacancy agree with the antisymmetric and symmetric stretching values of the free  $\text{CO}_3^{2-}$  ion; however, the calculated symmetric stretching is slightly lower for  $\text{CeO}_2(111)\text{vacO}$  with the oxygen of the  $\text{CO}_2$  molecule occupying the hole (Tables 3 and 4). This behavior can be attributed to the distorted  $\text{CO}_3^{2-}$  bond distances, as reported in Table 2. Remarkably, despite the resemblance of their geometries to the geometry of free carbonate, superficial

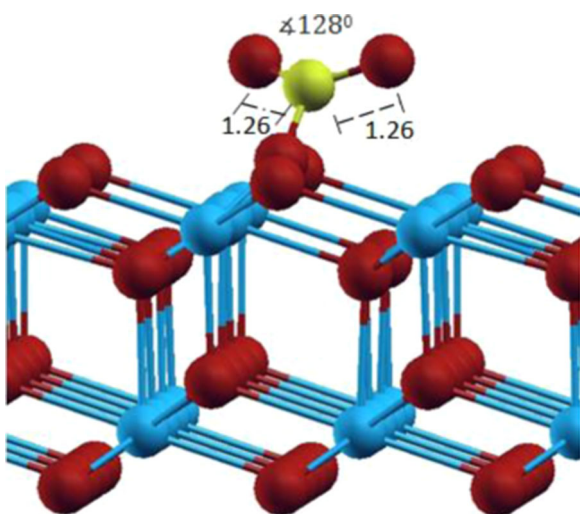


**Fig. 7** Adsorption of  $\text{CO}_2$  onto the  $\text{CeO}_2(111)\text{vacO}$  surface. Blue spheres Ce atoms, red spheres O atoms, yellow spheres C atoms. Interatomic distances are in Å

cerium carbonates are extremely stable and cannot be removed by heating [61]. On the other hand, on  $\text{ZnO}(0001)\text{vacO}$  surface, the  $\text{CO}_2$  adsorbs keeping the free molecule structure with one O atom occupying the O-vacancy place (see Fig. 8).

## $\text{H}_2$ adsorption

The geometric configurations of the  $\text{H}_2$  molecule on the  $\text{CeO}_2$  and  $\text{ZnO}$  surfaces with and without defects studied in the present work are similar, as are the stretching frequency values of the  $\text{H}_2$  molecule on those surfaces, and these results indicate weak interactions of  $\text{H}_2$  with these surfaces (see Fig. 9). Even though the  $\text{H}_2$  molecule is physisorbed at all of the surfaces, the strongest interaction occurs on the  $\text{CeO}_2(111)\text{vacO}$  surface, where the H–H bond length increases from 0.77 Å (for the free molecule) to 0.82 Å (see Fig. 10). This lengthening shifts the stretching frequency,  $\nu_{\text{H-H}}$ , down by  $\sim 1,200\text{ cm}^{-1}$  with respect to the free  $\text{H}_2$  (see Tables 3 and 4). Notice that the lengthening of the H–H bond occurs because of the charge transfer from the substrate to the antibonding  $\sigma^*(\text{H-H})$  orbital. The other  $\nu_{\text{H-H}}$  values are only slightly affected by the interactions with the surfaces, showing downshifts of less than  $\sim 200\text{ cm}^{-1}$ .

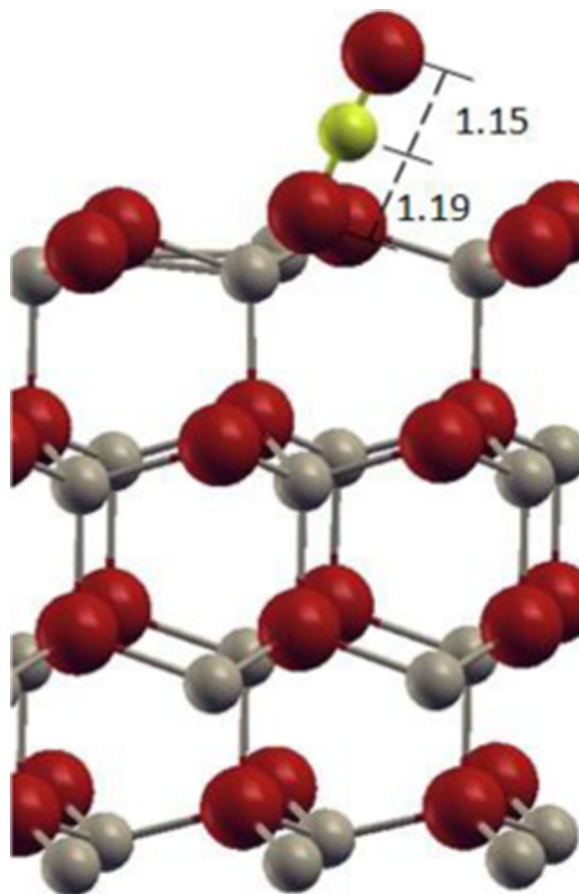


**Fig. 8** Adsorption of  $\text{CO}_2$  onto the  $\text{ZnO}(0001)\text{vacO}$  surface. Gray spheres Zn atoms, red spheres O atoms, yellow spheres C atoms. Interatomic distances are in Å



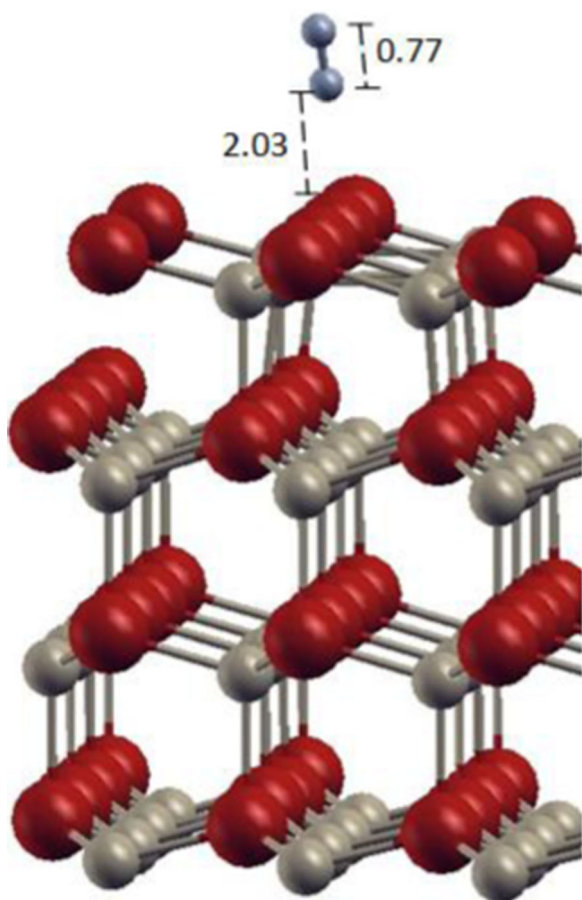


**Fig. 9** Adsorption of  $\text{H}_2$  onto the  $\text{ZnO}(0001)\text{vacO}$  surface. Gray spheres Zn atoms, red spheres O atoms, white spheres H atoms. Interatomic distances are in Å

We wish to underline here that the ZnO and ceria surfaces studied here do not break the H–H bond, in contrast to what was shown to occur on gallia surfaces with oxygen vacancies,  $\text{Ga}_2\text{O}_3(100)\text{vacO}$ , as well as on a monolayer of gallia on ceria  $\text{Ga}_2\text{O}_3/\text{Ce}_2\text{O}_3(111)$  [38], which is in close

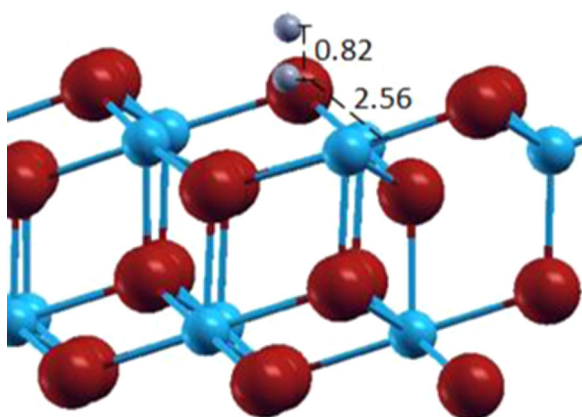


**Fig. 10** Adsorption of  $\text{H}_2$  onto the  $\text{CeO}_2(111)\text{vacO}$  surface. Blue spheres Ce atoms, red spheres O atoms, white spheres H atoms. Interatomic distances are in Å

agreement with the recently reported [62] enhanced reducibility (and improved redox properties) of the latter mixed oxide.

## Conclusions

The adsorption of CO is especially weak on perfect ceria surfaces, and the  $\text{Ce}(111)$  surface only shows some reactivity when it has oxygen vacancies and when the C atom of the CO is located at the vacancy. A noticeable lengthening effect on the C–O bond length was found to be caused by the adsorption process; such an effect is typical of a strong charge-transfer interaction from the substrate to the antibonding  $\sigma^*(\text{C}-\text{O})$  orbital. In addition, significant (down)shifts in the  $\nu_{\text{C}-\text{O}}$  values with respect to that of the free molecule on  $\text{CeO}_2(111)\text{vacO}$  were observed. By contrast,  $\text{ZnO}(0001)$  and  $\text{ZnO}/\text{CeO}_2(111)$  surfaces are very reactive towards CO, which uses a surface oxygen atom to generate a  $\text{CO}_2$  molecule.

Ceria surfaces are substantially more reactive than ZnO towards  $\text{CO}_2$ . This reaction yields planar  $\text{CO}_3^{2-}$  species. The highest adsorption energies were found for the adsorption of carbon dioxide onto  $\text{CeO}_2(111)\text{vacO}$ , with either the C atom linked to a surface O or any of the oxygen atoms of the  $\text{CO}_2$  molecule occupying the hole generated by the oxygen vacancy. In such cases, the  $\text{CO}_2$  accepts the electron pair from the hole, adopts the planar geometry of the  $\text{CO}_3^{2-}$  ion, and presents an angle of  $\sim 120\text{--}128^\circ$  between the oxygen atoms. The calculated  $\nu_{\text{C}-\text{O}}$  values on  $\text{CeO}_2(111)\text{vacO}$  agree fairly well with the antisymmetric and symmetric stretching values of the free  $\text{CO}_3^{2-}$ .

Molecular hydrogen does not exhibit significant interactions with  $\text{CeO}_2$  and ZnO surfaces, whether or not oxygen defects are present. Even though the  $\text{H}_2$  molecule is slightly physisorbed onto all of these surfaces, the strongest interaction occurs at one site on  $\text{CeO}_2(111)\text{vacO}$ , where the H–H bond length increases by  $\sim 0.05$  Å with respect to that of the free molecule. However, a significant downshift of  $\sim 1,200\text{ cm}^{-1}$  in the stretching frequency of the adsorbate,  $\nu_{\text{H}-\text{H}}$ , was found in this case.

**Acknowledgments** The authors thank Universidad Nacional del Sur (UNS), Universidad Nacional del Litoral (UNL), Consejo Nacional de Investigaciones Científicas y Técnicas (CONICET), and Agencia Nacional de Promoción Científica y Tecnológica (ANPCyT) for their continued financial support.

## References

1. United Nations (2014) Framework Convention on Climate Change. <https://www.unfccc.int>
2. Olah GA, Goepfert A, Surya Prakash GK (2009) Chemical recycling of carbon dioxide to methanol and dimethyl ether: from greenhouse



- gas to renewable, environmentally carbon neutral fuels and synthetic hydrocarbons. *J Org Chem* 74(2):487–498
3. Vancoillie J, Demuyneck J, Sileghem L, Van de Ginste M, Verhelst S (2012) Comparison of the renewable transportation fuels, hydrogen and methanol formed from hydrogen, with gasoline. *Int J Hydrog Energy* 37(12):9914–9924
  4. Sá S, Silva H, Brandão L, Sousa JM, Mendes A (2010) Catalysts for methanol steam reforming. *Appl Catal B Environ* 99:43–57
  5. Hsu WD, Ichihashi T, Kondow T, Sinnott SB (2007) Ab initio molecular dynamics study of methanol adsorption on copper clusters. *J Phys Chem A* 111:441–449
  6. Dunn S (2002) Hydrogen futures: toward a sustainable energy system. *Int J Hydrog Energy* 27:235–234
  7. Palo DR, Dagle RA, Holladay JA (2007) Methanol steam reforming for hydrogen production. *Chem Rev* 107(10):3992–4021
  8. Bonivardi AL, Chiavassa DL, Baltanás MA (1998) Promoting effect of calcium addition to Pd/SiO<sub>2</sub> catalysts in CO<sub>2</sub> hydrogenation to methanol. *Stud Surf Sci Catal* 114:533–536
  9. Bonivardi AL, Chiavassa DL, Querini CA, Baltanás MA (2000) Enhancement of the catalytic performance to methanol synthesis from CO<sub>2</sub>/H<sub>2</sub> by gallium addition to palladium/silica catalysts. *Stud Surf Sci Catal* 130:3747–3752
  10. Collins SE, Baltanás MA, García Fierro JL, Bonivardi AL (2002) Gallium–hydrogen bond formation on gallium and gallium–palladium silica-supported catalysts. *J Catal* 211:252–264
  11. Collins SE, Baltanás MA, Bonivardi AL (2004) An infrared study of the intermediates of methanol synthesis from carbon dioxide over Pd/β-Ga<sub>2</sub>O<sub>3</sub>. *J Catal* 226:410–421
  12. Chiavassa DL, Collins SE, Bonivardi AL, Baltanás MA (2009) Methanol synthesis from CO<sub>2</sub>/H<sub>2</sub> using Ga<sub>2</sub>O<sub>3</sub>-Pd/silica catalysts: kinetic modelling. *Chem Eng J* 150:204–212
  13. Armbrüster M, Behrens M, Fottinger K, Friedrich M, Gaudry E, Matam SK, Sharma HR (2013) The intermetallic compound ZnPd and its role in methanol steam reforming. *Catal Rev Sci Eng* 55:289–367
  14. Iwasa N, Yoshikawa M, Nomura W, Arai M (2005) Transformation of methanol in the presence of steam and oxygen over ZnO-supported transition metal catalysts under steam reforming conditions. *Appl Catal A Gen* 292:215–222
  15. Zhang Q, Farrauto RJ (2011) Methanol steam reforming catalyst for portable power applications. *Appl Catal A Gen* 395:64–70
  16. Ilinich O, Liu Y, Waterman EM, Farrauto RJ (2013) Kinetics of methanol steam reforming with a Pd-Zn-Y/CeO<sub>2</sub> catalyst under realistic operating conditions of a portable reformer in fuel cell applications. *Ind Eng Chem Res* 52:638–644
  17. Chuasiripattana K, Warschkow O, Delley B, Stampfl C (2010) Reaction intermediates of methanol synthesis and water-gas shift reaction on the ZnO(0001) surface. *Surf Sci* 604:1742–1751
  18. Kiss J, Frenzel J, Meyer B, Marx D (2013) Methanol synthesis on ZnO(0001). II. Structure, energetic, and vibrational signature of reaction intermediates. *J Chem Phys* 139(1–17):44705
  19. Kurtz M, Strunk J, Hinrichsen O, Muhler M, Fink K, Meyer B, Wöll C (2005) Aktive zentren an oxidoberflächen: Die ZnO-katalysierte methanol-synthese. *Angew Chem* 117:2850–2854
  20. Chinchin GC, Denny PJ, Parker DG, Spencer MS, Whan DA (1987) Mechanism of methanol synthesis from CO<sub>2</sub>/CO/H<sub>2</sub> mixture over copper/zinc oxide/alumina catalysts. *Appl Catal* 30:333–338
  21. Martins JBL, Taft CA (1997) Ab initio study of CO and H<sub>2</sub> interaction on ZnO surfaces using a small cluster model. *J Mol Struct* 398–399:457–466
  22. Martins JBL, Longo E, Rodriguez Salmon OD, Espinoza VAA, Taft CA (2004) The interaction of H<sub>2</sub>, CO, CO<sub>2</sub>, H<sub>2</sub>O and NH<sub>3</sub> on ZnO surfaces: an Oniom study. *Chem Phys Lett* 400:481–486
  23. Yao HC, Yao YFC (1984) Ceria in automotive exhaust catalysts: I. Oxygen storage. *J Catal* 86:254–260
  24. Taylor KC (1984) Catalysis in catalytic converters. In: Anderson JR, Boudart M (eds) *Catalysis science and technology*, vol 5. Springer, Berlin, pp 119–170
  25. Trovarelli C, De Leitenburg M, Boaro DG (1999) The utilization of ceria in industrial catalysis. *Catal Today* 50:353–367
  26. Conesa JC (1995) Computer modeling of surfaces and defects on cerium dioxide. *Surf Sci* 339:337–352
  27. Gennard S, Cora F, Catlow CRA (1999) Comparison of the bulk and surface properties of ceria and zirconia by ab initio investigations. *J Phys Chem B* 103(46):10158–10170
  28. Skorodumova N, Baudin M, Hermansson K (2004) Surface properties of ceria from first principles. *Phys Rev B* 69(1–8):075401
  29. Hay PJ, Martin RL, Uddin J, Scuseria GE (2006) Theoretical study of CeO<sub>2</sub> and Ce<sub>2</sub>O<sub>3</sub> using a screened hybrid density functional. *J Chem Phys* 125(1–8):034712
  30. Chen H-T, Choi YM, Liu M, Lin MC (2007) A theoretical study of surface reduction mechanisms of CeO<sub>2</sub>(111) and (110) by H<sub>2</sub>. *ChemPhysChem* 8:849–855
  31. Da Silva JLF, Ganduglia-Pirovano MV, Sauer J, Bayer V, Kresse G (2007) Hybrid functionals applied to rare-earth oxides: the example of ceria. *Phys Rev B* 75(1–10):045121
  32. Loschen C, Carrasco J, Neyman KM, Illas F (2007) First principles LDA + U and GGA + U study of cerium oxides: dependence on the effective U-parameter. *Phys Rev B* 75(1–8):035115
  33. Castleton CWM, Kullgren J, Hermansson K (2007) Tuning LDA + U for electron localization and structure at oxygen vacancies in ceria. *J Chem Phys* 127(1–11):244704
  34. Branda MM, Loschen C, Neyman KM, Illas F (2008) Atomic and electronic structure of cerium oxide stepped model surfaces. *J Phys Chem C* 112:17643–17651
  35. Burow AM, Wende T, Sierka M, Włodarczyk R, Sauer J, Claes P, Jiang L, Meijer G, Lievens P, Asmis KR (2011) Structures and vibrational spectroscopy of partially reduced gas-phase cerium oxide clusters. *Phys Chem Chem Phys* 13:19393–19400
  36. Lu D, Liu P (2014) Rationalization of the Hubbard U parameter in CeO<sub>x</sub> from first principles: unveiling the role of local structure in screening. *J Chem Phys* 140(1–7):084101
  37. Farra R, Wrabetz S, Schuster ME, Stotz E, Hamilton NG, Amrute AP, Pérez-Ramírez J, López N, Teschner D (2013) Understanding CeO<sub>2</sub> as a deacon catalyst by probe molecule adsorption and in situ infrared characterizations. *Phys Chem Chem Phys* 15:3454–3465
  38. Cheng Z, Sherman BJ, Lo C (2013) Carbon dioxide activation and dissociation on ceria (110): a density functional theory study. *J Chem Phys* 014702(1–12)
  39. Huang M, Fabris S (2008) CO adsorption and oxidation on ceria surfaces from DFT + U calculations. *J Phys Chem C* 112:8643–8648
  40. Branda MM, Ferullo RM, Causá M, Illas F (2011) Relative stabilities of low index and stepped CeO<sub>2</sub> surfaces from hybrid and GGA + U implementations of density functional theory. *J Phys Chem C* 115: 3716–3721
  41. Blöchl PE (1994) Projector augmented wave method. *Phys Rev B* 50: 17953–17979
  42. Monkhorst HJ, Pack JD (1976) On special points for Brillouin zone integrations. *Phys Rev B* 13:5188–5192
  43. Petit L, Svane A, Szotek Z, Temmerman WM (2005) First-principles study of rare-earth oxides. *Phys Rev B* 72:205118–205127
  44. Gerward L, Olsen JS, Petit L, Vaitheeswaran G, Kanchana V, Svane A (2005) Bulk modulus of CeO<sub>2</sub> and PrO<sub>2</sub>: an experimental and theoretical study. *J Alloys Compd* 400:56–61
  45. Anisimov VI, Aryasetiawan F, Lichtenstein AI (1997) First-principles calculations of the electronic structure and spectra of strongly correlated systems: the LDA + U method. *J Phys Condens Matter* 9:767–808
  46. Anisimov VI, Solov'yev IV, Korotin MA, Czyzyk MT, Sawatzky GA (1993) Density-functional theory and NiO photoemission spectra. *Phys Rev B* 48:16929–16934

47. Solovyev IV, Dederichs PH, Anisimov VI (1994) Corrected atomic limit in the local-density approximation and the electronic structure of *d* impurities in Rb. *Phys Rev B* 50:16861–16871
48. Loschen C, Migani A, Bromley ST, Illas F, Neyman KM (2008) Density functional studies of model cerium oxide nanoparticles. *Phys Chem Chem Phys* 10:5730–5738
49. Migani A, Neyman KM, Illas F, Bromley ST (2009) Exploring Ce<sup>3+</sup>/Ce<sup>4+</sup> cation ordering in reduced ceria nanoparticles using interionic potential and density functional calculations. *J Chem Phys* 131(1–7): 064701
50. Reimers WG, Baltanás MA, Branda MM (2013) Theoretical study on the reactivity of the surface of pure oxides: the influence of the support and oxygen vacancies. *Appl Surf Sci* 274:1–6
51. Methfessel M, Paxton AT (1989) High-precision sampling for Brillouin-zone integration in metals. *Phys Rev B* 40:3616–3621
52. Kresse G, Hafner J (1993) Ab initio molecular dynamics for liquid metals. *Phys Rev B* 47:558–561
53. Kresse G, Hafner J (1993) Ab initio molecular dynamics for open-shell transition metals. *Phys Rev B* 48:13115–13118
54. Kresse G, Hafner J (1994) Ab initio molecular-dynamics simulation of the liquid-metal–amorphous-semiconductor transition in germanium. *Phys Rev B* 49:14251
55. Kresse G, Furthmüller J (1996) Efficient iterative schemes for ab initio total-energy calculations using a plane-wave basis set. *Phys Rev B* 54:11169
56. Kresse G, Furthmüller J (1996) Efficiency of ab-initio total energy calculations for metals and semiconductors using a plane-wave basis set. *Comput Mater Sci* 6:15–50
57. Neugebauer J, Scheffler M (1992) Adsorbate–substrate and adsorbate–adsorbate interactions of Na and K adlayers on Al(111). *Phys Rev B* 46:16067–16080
58. Makov G, Payne MC (1995) Periodic boundary conditions in ab initio calculations. *Phys Rev B* 51:4014–4022
59. National Institute of Standards and Technology (2011) NIST Chemistry WebBook. <http://webbook.nist.gov>
60. Peralta JE, Ruiz de Azúa MC, Contreras RH (1999) Natural bond orbitals analysis of C–H–O interactions in NCH/H<sub>2</sub>O and NCH/OCH<sub>2</sub>, and their effect on nuclear magnetic shielding constants. *J Mol Struct THEOCHEM* 491:23–31
61. Trovarelli A (2002) Catalysis by ceria and related catalysts. *Catalytic Science Series*, vol 2. Imperial College, London
62. Vecchietti J, Collins S, Xu W, Barrio L, Stacchiola D, Calatayud M, Tielens F, Delgado JJ, Bonivardi A (2013) Surface reduction mechanism of cerium-gallium mixed oxides with enhanced redox properties. *J Phys Chem C* 117(17):8822–8831